Journal of Solar Energy Research (JSER)

Journal homepage: www.jser.ut.ac.ir

Numerical Multi-Variable Investigation and Optimization of a High-Temperature Hydrogen Production Process Using Solar-Based Heliostat Field and Supercritical CO_2 Utilization

Hassan Athari, Maghsoud Abdollahi Haghghi *

Department of Mechanical Engineering, Elm-o-Fann University College of Science and Technology, Urmia, Iran

Received: 02-12-2022
Accepted: 22-12-2022

Abstract

With regard to the sustainability of using carbon dioxide in supercritical processes, this study proposes a novel power/hydrogen cogeneration arrangement consisting of a recompression supercritical carbon dioxide gas turbine cycle and a solid oxide water electrolysis unit in integration with a high-temperature solar-based heliostat field. The steady operation of the system is also guaranteed by means of thermal energy storage tanks. On this path, a numerical multi-variable study and optimization of the entire system are conducted. Hence, four main parameters are viewed to study the sensitivity of the net power output, hydrogen output, energy and exergy efficiencies, and unit cost of products. Hence, a genetic algorithm is applied to investigate the optimum conditions of the entire system considering the maximum energy and exergy efficiencies and the minimum unit cost of products as objective functions. Looking at the results, the sensitivity of the outcomes is further affected by the increase in compressor 1 inlet pressure. Besides, the optimum energy efficiency is 26.81%, optimum exergy efficiency is 21.03%, and optimum unit cost of products is 18.79 $/GJ are attainable.

Keywords: Supercritical CO_2 utilization; Solar-based heliostat field; Solid oxide water electrolysis; Multi-variable investigation; Optimization

DOI: 10.22059/jser.2022.351972.1268 DOR: 20.1001.1.25883097.2023.8.1.7.3

1. Introduction

Transitioning from conventional energy conversion routes to updated technologies is absolutely needed to supply the energy demand in different sectors, i.e., urban, industrial, agricultural, etc. [1-3]. Renewable energy-based programs are incredibly increased in recent years; however, further attention is required to identify the most suitable way of energy conversation using renewable energy resources [4,5]. Solar energy is recognized as the zero-emission source of renewable heat-based energy utilized in many projects throughout the world. Different technologies, from low-temperature to high-temperature applications, have been built and evaluated in which high-temperature ones are appropriate for power plants. Solar power tower technology composed of heliostat mirrors and a central receiver is a proper selection for potential cities for power generation and other

*Corresponding Author Email Address:st_m.abdollahihaghi@urmia.ac.ir

multigeneration goals [6-9]. To highlight its application, a detailed literature review is represented in the following.

Sezer et al. [10] regarded and studied the advantages of a solar-based heliostat field (SHF) combined with wind turbines for simulation production of heating, cooling, power, and freshwater. They showed an exergy efficiency of 48%. Zoghi et al. [11] evaluated the exergy and cost aspects of integrating a SHF, a biomass gasification subsystem, a gas turbine cycle, low-temperature water electrolysis (LTWE) for hydrogen production, and cooling and heating terminals. So, an exergy efficiency of 43.1% and a total cost rate of products of 7799 $/h were found. Using a SHF, Yuksel et al. [12] investigated a multigeneration process for the simultaneous production of power, hydrogen, freshwater, cooling, and heating. The proposed system had a higher performance at higher ambient temperatures. Colakoglu and Durmayaz [13] showed the exergy and cost potential of a SHF combined with a gas turbine cycle. The result indicated an exergy efficiency of 34.5% and a levelized cost of products of 0.079 $/kWh. Considering a case study for Qatar, Nedaei et al. [14] proposed a multigeneration process relying on a SHF with net output power and exergy efficiency of 7.4 MW and 38.7%, respectively. Wang et al. [15] showed a thermal efficiency between 19.2% and 22% for a SHF integrated with a two-stage recompression gas turbine cycle. In a study by Liang et al. [16], a SHF was used to launch a two-stage recompression supercritical carbon dioxide (S-CO_2) gas turbine cycle combined with an organic Rankine cycle (ORC). The most suitable range of net power output was deduced between 2200 kW and 2300 kW. Sachdeva and Singh [17] examined the potential of a combined power plant encompassing a gas turbine cycle, an ORC, and a steam Rankine cycle (STC) in integration with a SHF. This arrangement indicated net power output of 332 kW per unit mass rate of input air of the gas turbine cycle. In a study by Sadeghi et al. [18], the applicability of a SHF combined with a multigeneration system producing power, heating, hydrogen, and oxygen was assessed and investigated. Through the study, they obtained an energy efficiency of 50% and an exergy efficiency of 45%. Keshavarzzadeh et al. [19] designed a SHF combined with a gas turbine cycle for a multigeneration application. They also optimized the operation and found that the optimum unit cost of products was 0.045 $/kWh. Khatoon and Kim [20] utilized supercritical and transcritical CO_2-based processes for power generation in combination with a SHF. So, the energy and exergy efficiencies of 42% and 67% were calculated, respectively. Yang et al. [21] used thermal energy storage for a SHF and provided the needed heat for a S-CO_2 gas turbine cycle. From their study, energy efficiency was available at 17.1% for winter and 17.8% for summer. Mohammadi et al. [22] considered a combustion chamber and a SHF to launch a recuperative gas turbine cycle. Besides, they stated that fuel consumption and emission decreased considerably.

Green hydrogen production is a valuable method of energy supply for remote areas, which can be considered within multigeneration processes [23-25]. Among available hydrogen production ways, water electrolysis, although an energy-intensive route, has great potential for environmentally friendly hydrogen generation [26-30]. A solid oxide electrolyzer cell (SOEC) is a high-temperature waster electrolyzer tool that is suitable for combined processes. Its applicability is reviewed in the following based on some recent studies [31]. Mohammadi and Mehrpooya [32] proposed a solar-based process using parabolic dish collectors for hydrogen generation through a SOEC and found that the hydrogen production rate per day and its cost were respectively equal to 41.48 kg/day and 9.1 $/kg. Wang et al. [33] proposed the use of an SOEC in integrating with an engine. The hydrogen production rate was found to be 22.39 kg/h. Hjeij et al. [34] designed a multigeneration process involving hydrogen production. The system also was capable to yield power, heating, ammonia, urea, and natural gas. The hydrogen production rate and total exergy efficiency were obtained to be 0.1 kg/s and 14%, respectively. Xu et al. [35] proposed and optimized a biomass-based steam Rankine cycle combined with a multi-effect desalination and a SOEC. The optimum exergy efficiency and unit cost of products were found to be 17.6% and 26 $/GJ, respectively. Using a SOEC, Alirahmi et al. [36] produced hydrogen via a geothermal-based multigeneration process. They showed that the optimum exergy efficiency was 37.9% and the optimum cost rate of products was 15.1 $/h.

Solar-based arrangements have been reviewed, where there is a gap in introducing high-temperature SOECs in combination with a SHF and S-CO_2 gas turbine cycle. On this account, this paper is prepared to design a novel framework for a power and hydrogen cogeneration system using a recompression S-CO_2 gas turbine cycle operated by

a SHF with thermal energy storage tanks and a SOEC. This study performs a sensitivity study from the thermodynamic and cost standpoints. In addition, a genetic algorithm is used to optimize the proposed process both thermodynamically and economically.

2. Process description

Figure 1 exhibits the schematic of the proposed arrangement in this study. As can be evident, three main parts are there, namely a SHF with storage tanks, a recompression S-CO_2 gas turbine cycle, and a SOEC. Since the highest operating temperature of the S-CO_2 process is lower than conventional gas turbine cycles, it can be regularly utilized in integration with a SHF. With regard to this ability, it can be represented that such process is proper because the change in the solar status affects the operation of such process less than gas turbine cycles.

First, low-pressure CO_2 flows into compressors 1 and 2 at states 1 and 13, respectively. Accordingly, flow 2 passing through the low-temperature recuperator (LTR) is mixed with flow 14 at state 3. So, flow 4 is made and enters the high-temperature recuperator (HTR). Consequently, the pressurized CO_2 is further warmed before flowing into the solar unit. Thus, flow 5 goes into storage tank 1 (St.T1), then flow 6 is delivered to the high-pressure turbine (HPT). Subsequently, flow 7 leaves the HPT and is reheated by using storage tank 2 (St.T5). Consequently, the heated CO2 is sent into the low-pressure turbine (LPT). Its output flow at state 9 is the hot flow entering the HTR and LTR. Considering state 18, the heated molten salt (59.5% LiCl / 40.5% KCl) flows into storage tanks at points 19 and 21. Subsequently, these flows are mixed at point 17 and the mixed flow is delivered to the receiver of the SHF. Here, 20% of the power produced by the supercritical process is considered for hydrogen production by the SOEC, and the rest is supplied to the grid.

In the SOEC, water at state 23 is pumped up to state 24, and this flow is delivered to heat exchanger 3 (HX3). Flow 24 is heated and enters the SOEC after crossing HX3, electrical steam generator (ESG), heat exchanger 2 (HX2), heat exchanger 1 (HX1), and electrical heater (EH), respectively. Subsequently, flow 29 is mixed with flow 33, and flow 30 is sent into the SOEC. Flow 32 is also sent into heat exchangers 1 and 3 for heat recovery; therefore, the yielded hydrogen is stored at state 35.

3. Materials and Methods

In order to simulate the proposed model, a code has been developed in the engineering equation solver (EES) software. Afterward, a genetic algorithm has been used to show the optimal operation of the system. EES is a general equation-solving software with the ability to solve thousands of coupled non-linear algebraic and differential equations numerically. Its other main features include solving differential and integral equations, do optimization, and provide uncertainty analyses. A major feature of EES is the high accuracy thermodynamic and transport property database that is provided for hundreds of substances in a manner that allows it to be used with the equation solving capability. The input conditions of the simulation are given in Table 1.

Table 1. Input data.

Input parameter	Value
SHF [37]	
DNI, kW/m^2	0.7
Optical efficiency, %	75
Outlet temperature of receiver, ℃	927
Speed of wind, m/s	5
Mirror^' s area, m^2	121
Central receiver area, m^2	60
Emissivity of absorber, (-)	0.88
Number of mirrors, (-)	280
Stefan–Boltzmann constant	5.67×10^{-8}
Recompression S-CO_2 cycle [38]	
Inlet temperature of HPT and LPT, ℃	677
PR of compressor, (-)	2.6
LPT's outlet pressure, bar	76
Isentropic efficiency of turbine, %	90
Isentropic efficiency of compressor, %	88
PPTD of LTR, ℃	5
PPTD of HTR, ℃	10
SOEC [39]	
Operating temperature, ℃	750
Base current density, A/cm^2	1
Outlet pressure, bar	1.15
Area of each cell, m^2	0.324
Pressure loss, %	3
Steam utilization factor, (-)	0.6
Thickness of anode, mm	17.5×10^{-3}
Thickness of cathode, mm	312.5×10^{-3}
Thickness of electrolyte, mm	12.5×10^{-3}
Pre-exponential factor of cathode,	1.344×10^{4}

A/cm^2	
Pre-exponential factor of anode, A/cm^2	2.051×10^3
Activation energy of anode, kJ/mol	120
Activation energy of cathode, kJ/mol	100
Effective diffusion coefficient at anode, m^2/s	2×10^{-5}
Effective diffusion coefficient at cathode, m^2/s	5.11×10^{-5}
Effectiveness of heat exchangers	0.97
Pump isentropic efficiency, %	80

Furthermore, some base assumptions are regarded as follows [37-39]:

- The temperature and pressure of the reference state are T_0 = 25 ºC and P_0 = 1 bar.
- The operation of the system is at steady-state.
- The pressure drop of the piping network and heat exchangers is zero.
- The kinetic and potential forms of energy and exergy are zero.
- Turbine, pumps, and compressors are adiabatically modelled with a specific isentropic efficiency.
- The operating temperature of the SOEC fixed.

3.1. Thermodynamic analysis

For each component, the mass balance equation and the first law of thermodynamics (energy balance) are mathematically given as [46]:

$$\dot{Q} - \dot{W} = \sum \dot{m}_{out} h_{out} - \sum \dot{m}_{in} h_{in} \quad (1)$$

$$\sum \dot{m}_{out} = \sum \dot{m}_{in} \quad (2)$$

where $\dot{m}$ denotes the mass flow rate, h denotes the

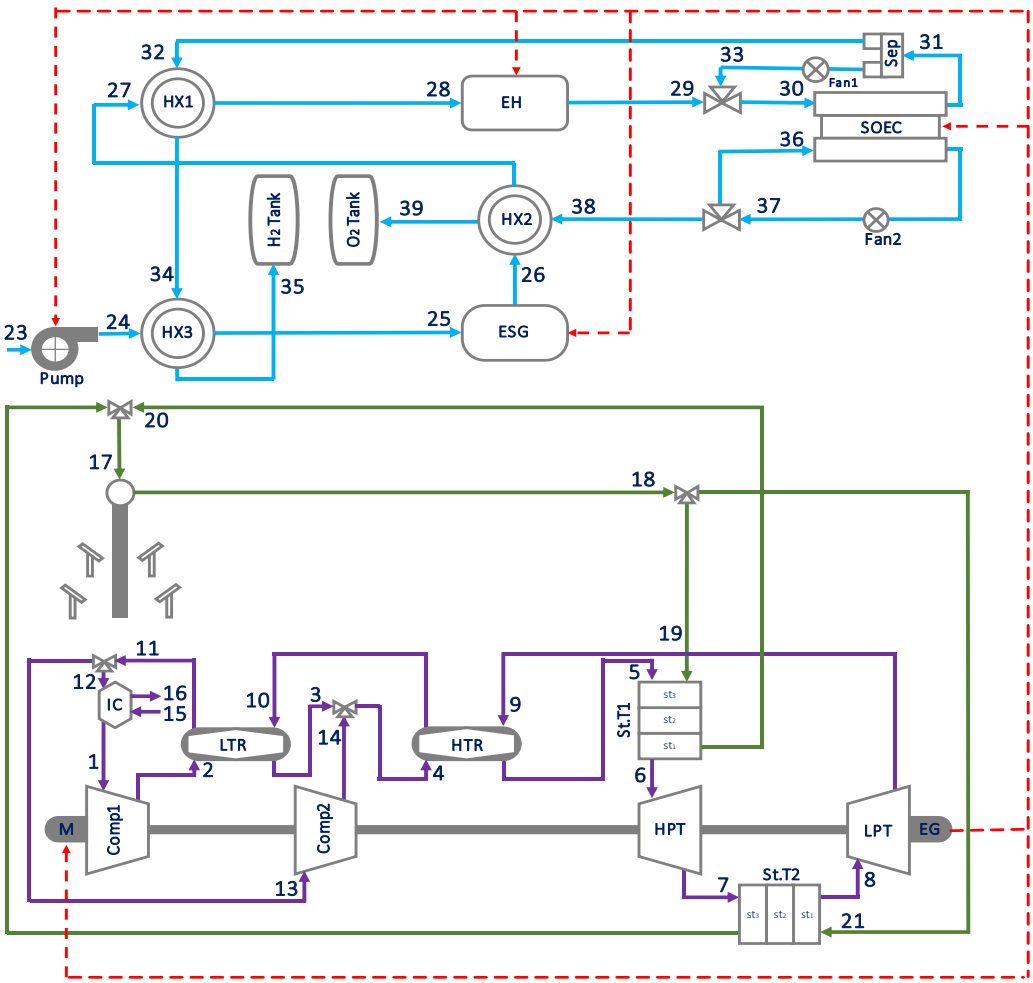

Figure 1. The schematic plot of the proposed power and hydrogen production system in this study.

specific enthalpy, $\dot{W}$ denotes the work, and $\dot{Q}$ denotes the heat transfer rate.

In addition, the second law of thermodynamics (exergy account) is formulated as [46]:

$$\dot{E}_d = \sum\left(1-\frac{T_0}{T_j}\right)\dot{Q}_j - \dot{W}_{cv} + \sum\dot{E}_{in} - \sum\dot{E}_{out} \quad (3)$$

where $\dot{E}_d$ denotes the exergy destruction rate.

Here, the exergy rate of each flow is calculable based on the physical ($\dot{E}_{ph}$) and chemical ($\dot{E}_{ch}$) exergy rates [46].

$$\dot{E} = \dot{E}_{ph} + \dot{E}_{ch} \quad (4)$$

$$\dot{E}_{ph} = \sum\dot{m}_i \times\left[\left(h_i - h_0\right) - T_0\left(s_i - s_0\right)\right] \quad (5)$$

$$\dot{E}_{ch} = \dot{n}\left[\sum y_m\,\bar{e}_m^{ch,0} + \bar{R}T_0\sum y_m\ln\left(y_m\right)\right] \quad (6)$$

Here, $\bar{R}$ denotes the universal gas constant, s denotes the specific entropy, y_m denotes the molar fraction of species m, and $\bar{e}_m^{ch,0}$ denotes its standard molar chemical exergy.

3.2. Solar-based heliostat field

The process of the SHF is definable via determining the solar input energy ($\dot{Q}_{SHF,in}$), gained useful energy ($\dot{Q}_{SHF,u}$), and energy loss ($\dot{Q}_{SHF,L}$). The rate of gained useful energy equals the difference between solar input energy and energy loss as follows [12,14,37]:

$$\dot{Q}_{SHF,u} = \dot{Q}_{SHF,in} - \dot{Q}_{SHF,L} \quad (7)$$

Here, the solar input energy is attainable by:

$$\dot{Q}_{SHF,in} = \eta_F DNI A_{mi} N_{mi} \quad (8)$$

where A_{mi} denotes the area of each mirror, N_{mi} denotes the number of mirrors, η_F denotes the optical efficiency, and DNI denotes the direct normal irradiation.

Here, energy loss depends on the radiation thermal loss ($\dot{Q}_{RAD}$), convection thermal loss ($\dot{Q}_{CONV}$), and reflection thermal loss ($\dot{Q}_{REF}$) [12,14,37].

$$\dot{Q}_{SHF,L} = \dot{Q}_{RAD} + \dot{Q}_{CONV} + \dot{Q}_{REF} \quad (9)$$

The radiation thermal loss is functioned as [12,14,37]:

$$\dot{Q}_{RAD} = \varepsilon\sigma A_{rec} F_r\left(T_{rec}^4 - T_a^4\right) \quad (10)$$

$$F_r = \frac{A_{ape}}{A_{rec}} \quad (11)$$

where σ denotes the Stefane-Boltzmann constant, $\boldsymbol{\varepsilon}$ denotes the emissivity coefficient, F_r denotes the view factor, T is the temperature, and A is the area. Here, subscript a, rec, and ape respectively denote ambient, receiver, and aperture.

Moreover, the convection thermal loss is defined as [12,14,37]:

$$\dot{Q}_{CONV} = h_{air,for,insi} A_{ape}\left(T_{rec} - T_a\right) \quad (12)$$

$$h_{air,for,insi} = 10.45 - V_{wind} + 10\sqrt{V_{wind}} \quad (13)$$

where $h_{air,for,insi}$ denotes the forced heat transfer coefficient and V_{wind} denotes the wind velocity.

Finally, reflection thermal loss equals:

$$\dot{Q}_{REF} = \dot{Q}_{SHF,in} F_r \rho_{rec} \quad (14)$$

where ρ_{rec} denotes the reflectivity coefficient of the receiver.

Referring to Ref. [40], storage tanks can be modelled in three different parts. Therefore, the following relations are utilized [40].

$$\frac{\rho V_{st}}{3} C_P \frac{dT_{st,1}}{dt} = \dot{m}_{MS} C_{P,MS}\left(T_{MS,in} - T_{st,1}\right) + \dot{m}_{CO_2} C_{P,CO_2}\left(T_{st,2} - T_{st,1}\right) - U_{st} A_{st,1}\left(T_{st,1} - T_a\right) \quad (15)$$

$$\frac{\rho V_{st}}{3} C_P \frac{dT_{st,2}}{dt} = \dot{m}_{MS} C_{P,MS}\left(T_{st,1} - T_{st,2}\right) + \dot{m}_{CO_2} C_{P,CO_2}\left(T_{st,3} - T_{st,2}\right) - U_{st} A_{st,2}\left(T_{st,2} - T_a\right) \quad (16)$$

$$\frac{\rho V_{st}}{3} C_P \frac{dT_{st,2}}{dt} = \dot{m}_{MS} C_{P,MS}\left(T_{st,2} - T_{st,3}\right) + \dot{m}_{CO_2} C_{P,CO_2}\left(T_{VG2,out} - T_{st,3}\right) - U_{st} A_{st,2}\left(T_{st,3} - T_a\right) \quad (17)$$

Based on Ref. [40], the unsteady terms in above-mentioned equations are neglectable.

Also [40],

$$T_{st,3} = T_{MS,out} \quad (18)$$

$$T_{st,1} = T_{CO_2,out} \quad (19)$$

In addition, the introduced areas are computed as [40]:

$$A_{st,1} = \frac{\pi D_{st}^2}{4} + \frac{\pi D_{st} L_{st}}{3} \quad (20)$$

$$A_{st,2} = \frac{\pi D_{st} L_{st}}{3} \quad (21)$$

$$A_{st,3} = \frac{\pi D_{st}^2}{4} + \frac{\pi D_{st} L_{st}}{3} \quad (22)$$

where [40]

$$L_{st} = \frac{D_{st}}{2} \quad (23)$$

$$V_{st} = \frac{A_{mi} N_{mi}}{30} \quad (24)$$

3.3. Solid oxide electrolyzer cell

The hydrogen production reaction of the SOEC is written as [39]:

$$H_2O \rightarrow 2H^+ + \frac{1}{2}O_2 + 2e^- \quad (25)$$

Hence, the molar rate of the hydrogen, water, and oxygen at the outlet state of the SOEC are formulated as [39]:

$$\dot{n}_{H_2,out} = \frac{J_{SOEC} N_{SOEC} A_{SOEC}}{2F} \quad (26)$$

$$\dot{n}_{O_2,out} = 0.5 \times \frac{J_{SOEC} N_{SOEC} A_{SOEC}}{2F} \quad (27)$$

$$\dot{n}_{H_2O,out} = \dot{n}_{H_2O,in} - \dot{n}_{H_2O,utilized} \quad (28)$$

$$\dot{n}_{H_2O,utilized} = \frac{J_{SOEC} N_{SOEC} A_{SOEC}}{2F} \quad (29)$$

where J_{SOEC} denotes the current density, A_{SOEC} denotes the cell area, N_{SOEC} denotes the number of cells, and F denotes the Faraday constant.

Additionally, the factor of steam utilization (U_{steam}) is crucial to perform the SOEC's molar balance. So, U_{steam} can be formulated as [39]:

$$U_{steam} = \frac{\dot{n}_{H_2O,utilized}}{\dot{n}_{H_2O,in}} \quad (30)$$

Afterward, cell voltage of the SOEC is fundable by the sum of the Nernest voltage (V_N) and voltage loss (V_L) [39]:

$$V_{SOEC} = V_N - V_L \quad (31)$$

where [39]

$$V_N = -\frac{\Delta \bar{g}^\circ}{2F} + \frac{\bar{R} T_{SOEC}}{2F} \ln\left(\frac{P_{O_2,an}^{0.5} P_{H_2,ca}}{P_{H_2O,ca}} \right) \quad (32)$$

$$\Delta \bar{g}^\circ = \bar{g}_{H_2O}^\circ - \bar{g}_{H_2}^\circ - 0.5 \bar{g}_{O_2}^\circ$$
$$\bar{g}^\circ = \bar{h} - T_{SOEC} \bar{s}^\circ \quad (33)$$

Here, $\Delta \bar{g}^\circ$ denotes the Gibbs free energy difference of the reaction and T_{SOEC} denotes the SOEC's operating temperature.

Also, the voltage loss equals [39]:

$$V_L = V_{ohm} + V_{act} + V_{conc} \quad (35)$$

Ohmic voltage (V_{ohm}) depends on the component i's thickness (δ_i), and constant variables A and B [39].

$$V_{ohm} = J_{SOEC} \cdot \left[A_i \delta_i \times exp\left(\frac{B_i}{T_{SOEC}} \right) \right] \quad (36)$$

The activation voltage loss (V_{act}) is available by [39]:

$$V_{act} = V_{act,a} + V_{act,c} \quad (37)$$

$$V_{act,a} = \frac{\bar{R} T_{SOEC}}{2F} \sinh^{-1}\left(\frac{J_{SOEC}}{2J_{o,a}} \right) \quad (38)$$

$$V_{act,c} = \frac{\bar{R} T_{SOEC}}{2F} \sinh^{-1}\left(\frac{J_{SOEC}}{2J_{o,c}} \right) \quad (39)$$

$$J_o = \gamma_i \exp\left(-\frac{E_{act}}{\bar{R} T_{SOEC}} \right) \quad (40)$$

where γ denotes the pre-exponential factor and J_o denotes the exchange current density.

Moreover, the concentration voltage loss (V_{conc}) is formulated as [39]:

$$V_{conc} = V_{conc,a} + V_{conc,c} \quad (41)$$

$$V_{conc,a} = \frac{\bar{R} T_{SOEC}}{2F} \ln\left[\left(1 + \frac{J_{SOEC} \bar{R} T_{SOEC} \delta_a}{2F D_a^{eff} P_{O_2,a}} \right)^{0.5} \right] \quad (42)$$

$$V_{conc,c} = \frac{\bar{R} T_{SOEC}}{2F} \ln\left(\frac{1 + \frac{J_{SOEC} \bar{R} T_{SOEC} \delta_c}{2F D_c^{eff} P_{H_2,c}}}{1 - \frac{J_{SOEC} \bar{R} T_{SOEC} \delta_c}{2F D_c^{eff} P_{H_2O,c}}} \right) \quad (43)$$

where D^{eff} denotes the effective diffusion coefficient.

Consequently, the required power by the SOEC is obtained as [39]:

$$\dot{W}_{SOEC} = N_{SOEC} J_{SOEC} A_{SOEC} V_{SOEC} \quad (44)$$

Its input power is provided from the recompression S-CO_2 gas turbine cycle and equals 20% of its net power output.

3.4. Thermoeconomic analysis

Thermoeconomics is a cost-based evaluation method suitable for energy systems based on the exergy, total investment cost ($\dot{Z}_{tot}$), and cost of input fuel ($\dot{C}_{fuel}$).

The total investment cost is definable as the sum of the investment cost of all components.

For a known component, the investment cost is equal to [47]:

$$\dot{Z} = Z \frac{CRF}{N} \varphi \tag{45}$$

Here, Z denotes the purchase cost (see Table 2), CRF denotes the capital recovery factor, φ denotes the maintenance factor, and N denotes time of operation during the year.

CRF depends on the lifetime (n) and interest rate (i_r) of the system as follows [47]:

$$CRF = \frac{i_r \ (1+i_r \ )^n}{(1+i_r \ )^n \text{-} 1} \tag{46}$$

Table 2. Investment cost function of devises [41-43].

Device	Relevant equation
SHF	$Z_{SHF} = Z_{rec} + Z_{Hel}$
	$Z_{rec} = A_{rec} \left(79 \times T_{rec} - 42000\right)$
	$Z_{Hel} = 150 \times N_{mi} A_{mi}$
St.T	$Z_{St.T} = 494.09 + 808 \times V_{st.T}$
Tur	$Z_{tur} = \frac{479.34 \times \dot{m}_{in}}{0.92 - \eta_{GT}} \ln\left(\frac{P_{out}}{P_{in}}\right) \times \left[1 + \exp\left(0.036 \times T_{GT} - 54.4\right)\right]$
EG	$Z_{EG} = 26.18\left(\dot{W}_{EG}\right)^{0.95}$
Comp	$Z_{comp} = \frac{71.1 \times \dot{m}_{in} PR_{comp}}{0.9 - \eta_{AC_1}} \ln\left(PR_{comp}\right)$
Motor	$Z_M = 26.18\left(\dot{W}_M\right)^{0.95}$
Recu	$Z_R = 12000\left(\frac{A_R}{100}\right)^{0.6}$
SOEC	$Z_{SOEC} = A_{SOEC} N_{SOEC} \left(2.96 \times T_{SOEC} - 1907\right)$
HX	$Z_{HX} = 130\left(\frac{A_{HX}}{0.093}\right)^{0.78}$
IC	$Z_{IC} = 12000\left(\frac{A_{IC}}{100}\right)^{0.6}$
Pump	$Z_{pump} = 1266\left(\frac{\dot{W}_{pump}}{1000}\right)^{0.71}\left(1 + \frac{0.2}{1-\eta_{pump}}\right)$

Subsequently, the investment cost should be updated using the chemical index of the present year (CI_{PY}) and reference year (CI_{RY}) as below [47]:

$$\dot{Z}_{updated} = \dot{Z} \frac{CI_{PY}}{CI_{RY}} \tag{47}$$

3.5. Performance variables

The current study investigates five main performance variables formulated in the following.

First, the net power output equals [46]:

$$NPO = \dot{W}_{EG} - \dot{W}_M - \dot{W}_{SOEC} - \dot{W}_{ESG} - \dot{W}_{EH} - \dot{W}_{pump} \tag{48}$$

Also, the hydrogen output is found as [46]:

$$HO = 24 \times 3600 \times \frac{\dot{m}_{35}}{\rho_{H_2}} \tag{49}$$

Consequently, the energy and exergy efficiencies are obtainable as [46]:

$$\eta_{en} = \frac{NPO + \dot{m}_{35} LHV_{H_2}}{\eta_F DNIA_{mi} N_{mi}} \tag{50}$$

$$\eta_{ex} = \frac{NPO + \dot{m}_{35} e_{H_2}^{ch,0}}{DNIA_{mi} N_{mi} \left[1 + \left(\frac{1}{3}\right)\left(\frac{T_0}{T_s}\right)^4 - \left(\frac{4}{3}\right)\left(\frac{T_0}{T_s}\right)\right]} \tag{51}$$

Finally, products' unit cost of the system is equal to [47]:

$$c_{product} = \frac{\dot{Z}_{tot}}{NPO + \dot{E}_{35}} \tag{52}$$

3.6. Optimization

Optimizing the performance of energy systems to find an optimal balance between thermodynamic efficiency and costs can elicit cost reduction in addition to lasting stability. Accordingly, this part aims to present an optimization model to determine the optimal functioning of the system. Among different methods, herein the genetic algorithm structure as an evolutionary method is employed for optimizing the system [44]. Figure 2 shows the relevant flowchart. The genetic algorithm uses the natural selection process to solve constrained and unconstrained optimization problems, simulating

biological evolution. This algorithm alters the population of individual solutions iteratively. The genetic algorithm picks individuals at random from the existing population at each stage and employs them as parents to create offspring for the following generation [45]. The population "evolves" toward the best option over the course of subsequent generations. The algorithm is available for optimization via the EES software. The objective functions put forwards herein include overall energy efficiency (η_{en}), overall exergy efficiency (η_{ex}), unit cost of products and ($c_{product}$) of the system.

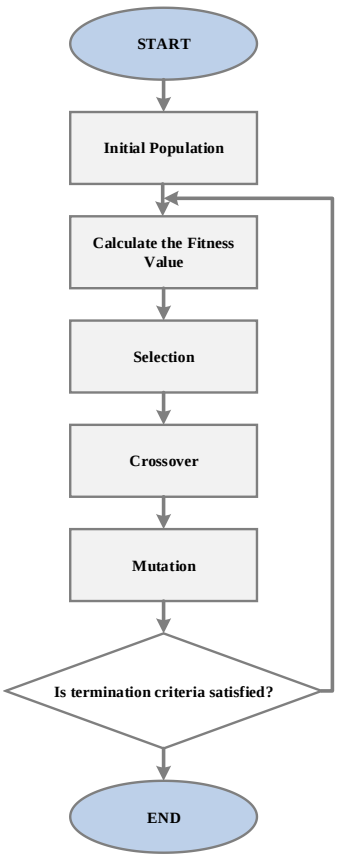

Figure 2. The flowchart of the genetic algorithm.

In this regard, the decision variables and their range of change are introduced below:

$$2.4 \le PR_{copm} \le 4 \ (-) \quad (53)$$

$$665 \le T_{in,tur} \le 710 \ (^{\circ}\mathrm{C}) \quad (54)$$

$$75 \le P_1 \le 90 \ (\mathrm{bar}) \quad (55)$$

$$0.4 \le J_{SOEC} \le 1.3 \ (\mathrm{A/cm^2}) \quad (56)$$

We considered a comprehensive parametric study and concluded that decision variables selected in equations 53-56 have the highest impact on the main objectives. So, these variables have been chosen for optimization. Also, we considered these parameters and their limitation range according to two main points. At first, we regarded similar studies; second to that, we considered the limitations of the simulation governing our new proposed system.

The optimization function is shown as follows if the objective function is decided to be the overall energy efficiency:

Maximize (EnOM): EnOM = η_{en} {Based on decision variables} (57)

If overall exergy efficiency is determined as the objective function, the optimization function is presented as:

Maximize (ExOM): ExOM = η_{ex} {Based on decision variables} (58)

If the $c_{product}$ is set as the objective function, then:

Minimize (COM): COM = $c_{product}$ {Based on decision variables} (59)

To do this, number of generations, number of individuals, mutation rate, and crossover are respectively set as 64, 32, 0.2, and 0.8, respectively.

4. Results and discussion

This section is provided in three parts, validation, sensitivity study, and optimization results.

4.1. Validation

Tables 3 and 4 respectively show the validity of the model of the SHF and SOEC in this study. As Table 3 depicts, the efficiency of the receiver is evaluated based on different solar irradiations and is compared with those reported by Xu et al. [37]. Here, the selected rang for the *DNI* is between 0.2 kW/m^2 and 1.0 kW/m^2, and the obtained total error is below 1%.

Table 3. Model validation of the SHF with Ref. [37].

DNI (kW/m^2)	This study	Ref. [37]
	η_{rec} (%)	
0.2	43.0	45.0
0.4	49.5	50.0
0.6	53.0	54.0

0.8	55.0	56.0
1.0	57.0	58.0

In addition, according to Table 4, the accurate simulation of the SOEC is visible. Here, the data obtained by AlZahrani and Dincer [39] are considered for validation. So, the model is verified by a total error below 1%.

Table 4. Model validation of the SOEC with Ref. [39].

J_{SOEC} (A/cm^2)	This study	Ref. [39]
	Power density (A/m^2)	
0.3	3.26	3.2
0.4	4.43	4.2
0.5	5.62	5.5
0.6	6.85	6.9
0.7	8.10	8.15
0.8	9.38	9.6
0.9	10.69	10.5
1.0	12.02	11.9

4.2. Parametric study

In the present work, the parametric study is performed with respect to the variation in important thermodynamic and thermoeconomic variables, including *NPO*, *HO*, η_{en}, η_{ex}, and $c_{product.}$ In addition, the studied parameters are given in equations 53-56. Plots 3-6 exhibit the pertinent results.

In Figure 3, the evaluated variables are measured against PR_{comp} ranging from 2.4 to 4. From Figures 3a and 3b, *NPO* increases and *HO* decreases. The increase in the PR_{comp} diminishes the CO_2 mass flow rate, so the power produced by the HPT goes up while LPT's capacity goes down. Due to the higher impact of the LPT's capacity on the *NPO*, this variable decreases from 3352 to 3273 kW. As previously pointed out, the SOEC subsystem receives its input power from the recompression S-CO_2 gas turbine cycle. Owing to the reduction in its power output, the rate of electrochemical reaction reduces; as a result, *HO* declines from 7080 to 9614 m^3/day. According to Figures 3b and 3c, both thermodynamic efficiencies, i.e., η_{en} and η_{ex}, face a drop. This trend strongly depends on the reduction in the level of products with PR_{comp}. Hence, η_{en} reduces from 23.89% to 23.33% and η_{ex} from 19.09% to 18.65%. From the economic perspective, as Figure 3d shows, higher evaluated pressure ratios are inappropriate by which the $c_{product}$ escalates from 20.78 to 21.37 $/GJ. This trend is a consequence of decreased exergy level of products.

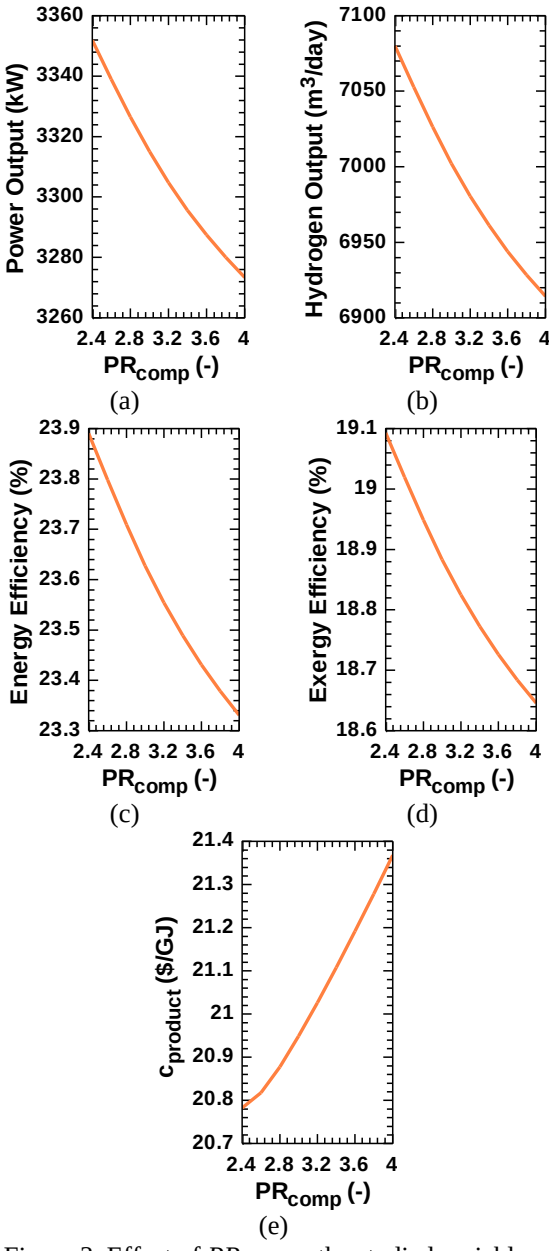

Figure 3. Effect of PR_{comp} on the studied variables.

The behaviour of the studied performance variables based on $T_{in,tur}$ (from 665 to 710 °C) is investigated in Figure 4. As can be seen, enhancing this variable positively affects the productivity and cost measures of performance. According to Figure 4a, although the enthalpy difference of both turbines increases affected by this change, the CO_2 mass flow rate drops. Therefore, the power yielded by turbines and power supplied to compressors decline.

However, the difference between the produced power and consumed power increases, so *NPO* experiences an increase from 3303 to 3429 kW. Consequently, the *HO* also enhances from 6977 to 7943 m^3/day (see Figure 4b). Higher productivity of products leads to proper thermodynamic performance at higher temperatures. As Figures 4c and 4d depict, η_{en} and η_{ex} increase from 23.45% and 18.81% to 24.44% and 19.53%, respectively. This means that the irreversibility of the system reduces with $T_{in,tur}$, so $c_{product}$ experiences a reduction from 21.10 to 20.12 $/GJ.

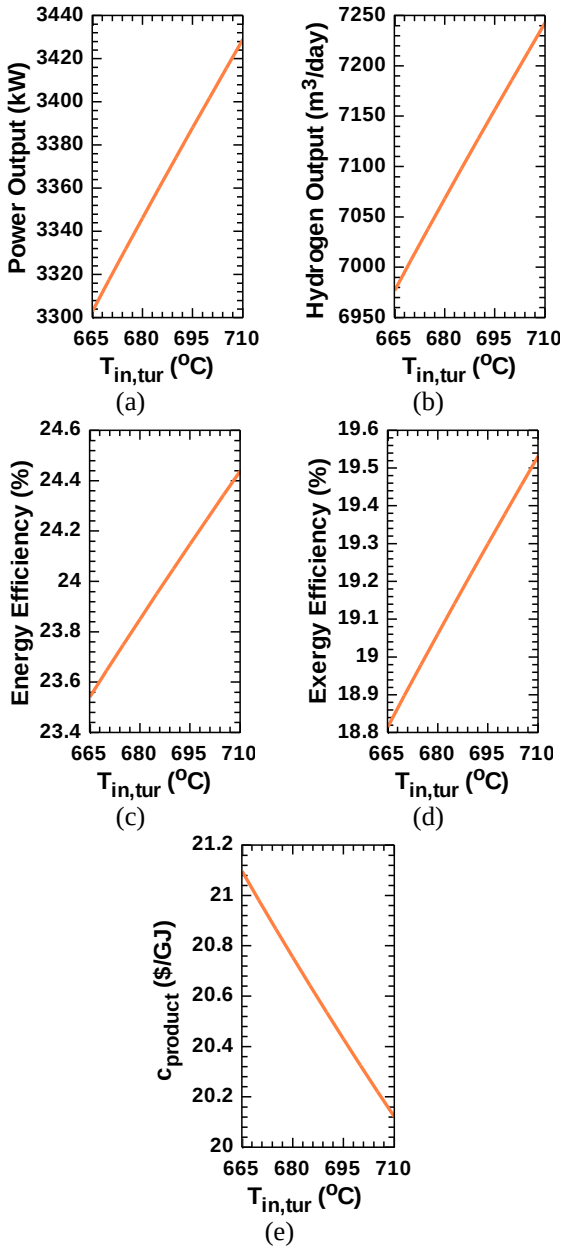

Figure 4. Effect of $T_{in,tur}$ on the studied variables.

The influence of increasing P_1 from 75 to 90 bar on the investigated performance variables is visible in Figure 5.

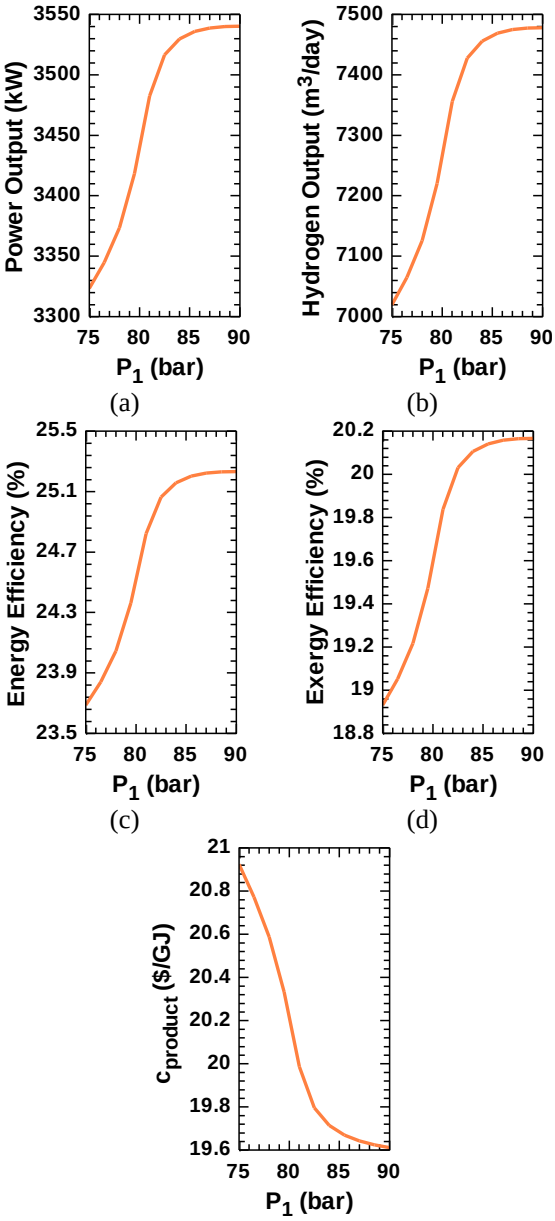

Figure 5. Effect of P_1 on the studied variables.

With this increase, the CO_2 mass flow rate at the outlet of the LPT upsurges. Also, the inlet mass flow rate of Comp1 decreases and of Comp2 increases, so their consumed power decreases and increases, respectively. Hence, the total power consumption capacity of the recompression S-CO_2 gas turbine cycle reduces. Furthermore, HPT is able to produce

further power with increasing P_1. Consequently, *NPO* rises from 3323 to 3540 kW, and *HO* from 7020 to 7478 m^3/day. Referring to Figures 5c and 5d, η_{en} and η_{ex} upsurge from 23.69% and 18.93% to 25.23% and 20.17%, correspondingly. From Figure 5e, it is deduced that higher pressures at state 1 cause lower $c_{product}$ because the exergy ability of the system enhances. So, $c_{product}$ declines from 20.92 to 19.61 $/GJ.

Figure 6 indicates the effect of the last studied parameter, i.e., J_{SOEC} (from 0.4 to 1.3 A/cm^2), on the performance variables. This variation affects *HO* at first owing to the variation in N_{SOEC} and V_L. Indeed, V_L enhances with growing the J_{SOEC}; however, because of the constant SOEC's power input, N_{SOEC} and the mass flow rate of the water input diminish, as well. Therefore, *HO* reduces from 7653 to 6818 m^3/day. Also, the power supplied to the ESG and EH witnesses a decrement, resulting an increment in the *NPO* from 3329 to 3340 kW. The reduced *HO* not only causes a reduction in energy and exergy levels of products, but also increases the irreversibility of the processes, so both efficiencies decline. Here, η_{en} and η_{ex} descend from 24.17% and 19.31% to 23.64% and 18.89%, correspondingly. Looking at Figure 5e, $c_{product}$ faces a slight reduction at first, then rises up to 20.91 $/GJ at 1.3 A/$cm^2$.

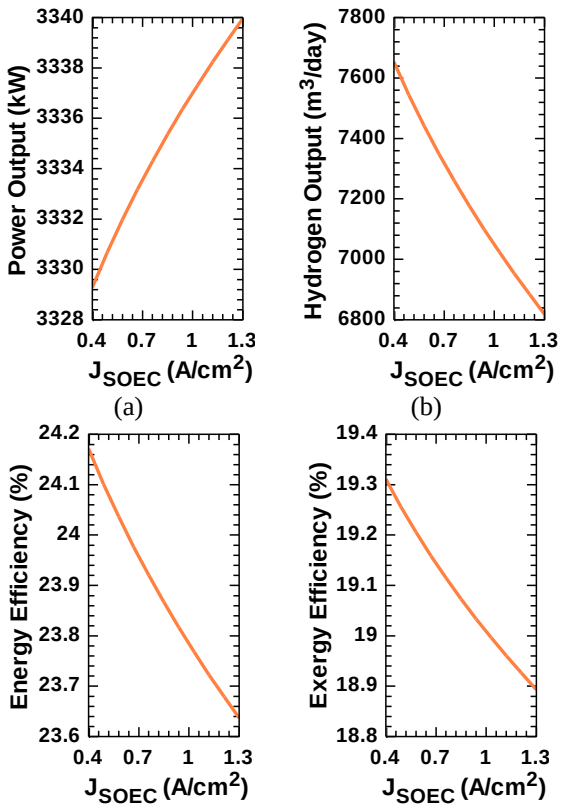

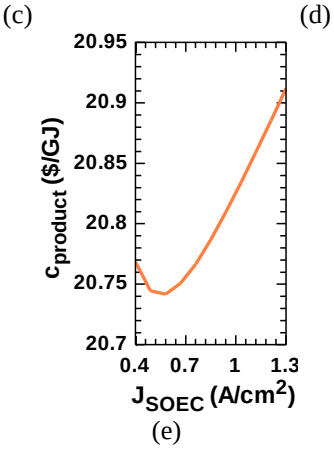

Figure 6. Effect of J_{SOEC} on the studied variables.

4.3. Optimization results

This study utilized a genetic algorithm to optimize the operation of the system in three different scenarios, namely EnOM, ExOM, and COM. The selected decision parameters are completely discussed in equations 53-56. Hence, Table 5 indicates the relevant outcomes. Based on this table, the η_{en} of the EnOM equals 26.81%; this variable is 3.03 percent-point higher than base case. Referring to the second case (ExOM), η_{ex} is obtained to be 21.03; 2.02 percent-point higher than base case. In the last case (COM), $c_{product}$ is found to be 18.79 $/GJ which is 9.8% better than the base case. The highest *NPO* is attained to be 3610 kW correspondent to the first optimum case. In addition, the highest *HO* is equal to 8266 m^3/day visible in the second optimization case (ExOM).

Table 5. Optimization results of decision parameters and performance variables.

Parameter	Base	EnOM	ExOM	COM
PR_{comp} (-)	2.63	3.21	3.32	3.43
$T_{in,tur}$ (°C)	676.9	708.9	709.9	709.9
P_1 (bar)	76.0	85.2	86.1	87.1
J_{SOEC} (A/cm^2)	1.00	0.41	0.40	0.53
NPO (kW)	3337	3610	3583	3410
HO (m^3/day)	7049	8221	8266	8079
η_{en} (%)	23.78	26.81	26.01	25.05
η_{ex} (%)	19.01	20.76	21.03	20.89
$\dot{Z}_{tot}$ ($/h)	315.6	319.1	317.2	313.5
$c_{product}$ ($/GJ)	20.83	19.28	18.99	18.79

Figure 7 indicates the results of the exergy destruction rate for established components of the

proposed system at the optimum state based on exergy efficiency (ExOM). As can be seen, the highest exergy destruction rate belongs to the HSF, where the total exergy destruction rate of this component is computed to be 20667 kW. After that, HTR and storage tank 1 have the second- and third-highest exergy destruction rates of 595.5 kW and 245.7 kW, respectively.

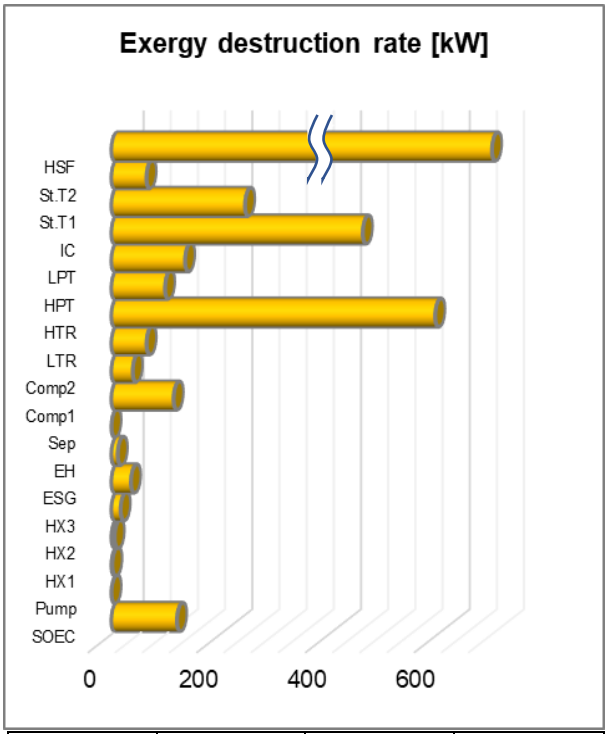

SOEC	120.5	Comp2	39.16
Pump	3.09E-05	LTR	64.51
HX1	1.584	HTR	595.5
HX2	5.806	HPT	98.54
HX3	16.79	LPT	135.4
ESG	35.83	IC	462.3
EH	11.52	St.T1	245.7
Sep	0	St.T2	64.43
Comp1	114.3	SHF	20667

Figure 7. Exergy destruction rate of components at ExOM mode.

5. Conclusions

This study presented an innovative high-temperature cogeneration system producing power and hydrogen using solar energy. The system comprised a solar-based heliostat field (SHF), a recompression supercritical carbon dioxide (S-CO_2) gas turbine cycle, and a solid oxide electrolyzer cell (SOEC). The proposed system was examined from thermodynamic and thermoeconomic points of view and optimized using a genetic algorithm. Three different optimization cases (EnOM, ExOM, and COM) are considered and evaluated. The main findings of the study are as follows:

- Referring to the parametric study, the sensitivity of the studied performance variables was more changed with increasing P_1.
- The increase in the PR_{comp} led to a decline in the production capacity of products and η_{en} and η_{ex}. Also, $c_{product}$ increased continuously.
- Higher $T_{in,tur}$ and P_1 were thermodynamically and economically useful. They increased the productivity, both efficiencies, and decreased the $c_{product}$.
- With increasing the J_{SOEC}, HO, η_{en}, and η_{ex} reduced, whereas NPO faces an increment. The $c_{product}$ declined at first, then increased.
- The optimum η_{en} was equals 26.81%; 3.03 percent-point higher than base case. Also, the optimum η_{ex} was 21.03; 2.02 percent-point higher than base case. Moreover, the optimum $c_{product}$ was calculated at 18.79 \$/GJ which is 9.8% better than the base case.

The most crucial limitations of the proposed design depend on the establishment and use of equipment and control of thermodynamic conditions. In detail, limited access to solar energy and unstable radiations can create problems for sustainable operation. On the other hand, reserved devices should be available to increase the life of the system and respond to specific conditions. Due to the structure of the system, expert supervisory workforces are also required permanently. In addition, from the thermodynamic operating conditions, controlling the solar status through storage tanks is critical for the stability of the proposed process.

For further studies, since the proposed process for the HSF subsystem has a high thermal-environmental potential compared to similar studies in the literature, it is suggested to investigate the use of available solar energy in each climatic with a case study approach. In addition, a life cycle assessment can be useful to show the performance of the proposed system completely.

Nomenclator

A	Area (m^2)
$c_{product}$	Unit cost of products (\$/GJ)

C_P	Specific heat capacity at constant pressure (kJ/kgK)
CRF	Capital recovery factor
CI	Chemical index
D_{st}	Diameter of the storage tank (m)
D^{eff}	Effective diffusion coefficient (m^2/s)
Δg	Gibbs free energy difference (kJ)
$\bar{e}_m^{ch,0}$	Standard molar chemical exergy (kJ/kmol)
F_r	View factor (-)
F	Faraday constant (C/mole)
h	Specific enthalpy (kJ/kg)
HO	Hydrogen output (m^3/day)
i_r	Interest rate (%)
J	Current density (A/cm^2)
J_0	Exchange current density (A/cm^2)
L_{st}	Length of the storage tank (m)
$\dot{m}$	Mass rate (kg/s)
n_r	System lifetime (year)
N	Yearly operational time (h)
N_{mi}	Number of mirrors
N_{SOEC}:	Number of cells
$\dot{n}$	Molar flow rate (mol/s)
P	Pressure (kPa)
PR_{comp}	Compressor pressure ratio,(-)
$\dot{Q}$	Heat transfer rate (kW)
$\bar{R}$	Universal gas constant (kJ/kmolK)
s	Specific entropy (kJ/kgK)
T	Temperature (^oC)
U_{st}	Thermal loss coefficient of the storage tank (kW/m^2K)
U_{steam}	Steam utilization factor (-)
V	Voltage (V)
V_{st}	Storage volume (m^3)
NPO	Net power output (kW)
Z	Purchase cost ($)
$\dot{Z}$	Cost rate of investment ($/h)

Greek Symbols

γ	Factor of pre-exponential (A/m^2)
δ	Thickness (mm)
ε:	Coefficient of emissivity (-)
η_F	Optical efficiency, (-)
η_{ex}	Exergy efficiency (%)
η_{en}	Energy efficiency (%)
ρ	Coefficient of reflectivity
σ	Stefane-Boltzmann constant
φ	Maintenance factor

Subscripts

A	Anode
act	Activation
ape	Aperture
c	Cathode
ch	Chemical
conc	Concentration
conv	Convection
in	Input
mi	Mirror
out	Output
ohm	Ohmic
ph	Physical
rad	Radiation
rec	Receiver
ref	Reflection
st	Storage tank
tot	Total
u	Useful

References

[1] Abdollahi Haghghi, M., Pesteei, S. M., & Chitsaz, A. (2018). Thermodynamic analysis of using parabolic trough solar collectors for power and heating generation at the engineering faculty of Urmia University in Iran. Journal of Solar Energy Research, 3(3), 187-200.

[2] Athari, H., Abdollahi Haghghi, M., Delpisheh, M., & Rahimi, Y. (2021). Assessment of wet compression integrated with air-film blade cooling

in gas turbine power plants. Journal of Solar Energy Research, 6(4), 913-922.

[3] Cao, Y., Dhahad, H. A., Togun, H., Haghghi, M. A., Athari, H., & Mohamed, A. M. (2021). Exergetic and economic assessments and multi-objective optimization of a modified solar-powered CCHP system with thermal energy storage. Journal of Building Engineering, 43, 102702.

[4] Haghghi, M. A., & Pesteei, S. M. (2017). Energy and exergy analysis of flat plate solar collector for three working fluids, under the same conditions. Progress in Solar Energy and Engineering Systems, 1(1), 1-9.

[5] Tyagi, H., Agarwal, A. K., Chakraborty, P. R., & Powar, S. (2019). Introduction to advances in solar energy research. In Advances in Solar Energy Research (pp. 3-11). Springer, Singapore.

[6] Abdollahi Haghghi, M., Pesteei, S. M., & Chitsaz Khoyi, A. (2019). Exergoeconomic analysis of a heating and power generation solar system for using at the engineering faculty of Urmia University. Modares Mechanical Engineering, 19(2), 415-427.

[7] Haghghi, M. A., Holagh, S. G., Pesteei, S. M., Chitsaz, A., & Talati, F. (2019). On the performance, economic, and environmental assessment of integrating a solar-based heating system with conventional heating equipment; a case study. Thermal Science and Engineering Progress, 13, 100392.

[8] Ghaffarzadeh, N., & Faramarzi, H. (2022). Optimal Solar plant placement using holomorphic embedded power Flow Considering the clustering technique in uncertainty analysis. Journal of Solar Energy Research, 7(1), 997-1007.

[9] Mbachu, V. M., Muogbo, A. G., Ezeanaka, O. S., Ejichukwu, E. O., & Ekwunife, T. D. (2022). An Economic Based Analysis of Fossil Fuel Powered Generator and Solar Photovoltaic System as Complementary Electricity Source for a University Student's Room. Journal of Solar Energy Research, 7(4), 1159-1173.

[10] Sezer, N., Biçer, Y., & Koç, M. (2019). Design and analysis of an integrated concentrated solar and wind energy system with storage. International Journal of Energy Research, 43(8), 3263-3283.

[11] Zoghi, M., Habibi, H., Choubari, A. Y., & Ehyaei, M. A. (2021). Exergoeconomic and environmental analyses of a novel multi-generation system including five subsystems for efficient waste heat recovery of a regenerative gas turbine cycle with hybridization of solar power tower and biomass gasifier. Energy Conversion and Management, 228, 113702.

[12] Yuksel, Y. E., Ozturk, M., & Dincer, I. (2019). Energetic and exergetic assessments of a novel solar power tower based multigeneration system with hydrogen production and liquefaction. International Journal of Hydrogen Energy, 44(26), 13071-13084.

[13] Colakoglu, M., & Durmayaz, A. (2022). Energy, exergy and economic analyses and multiobjective optimization of a novel solar multi-generation system for production of green hydrogen and other utilities. International Journal of Hydrogen Energy.

[14] Nedaei, N., Azizi, S., & Farshi, L. G. (2022). Performance assessment and multi-objective optimization of a multi-generation system based on solar tower power: A case study in Dubai, UAE. Process Safety and Environmental Protection, 161, 295-315.

[15] Wang, X., Liu, Q., Lei, J., Han, W., & Jin, H. (2018). Investigation of thermodynamic performances for two-stage recompression supercritical CO2 Brayton cycle with high temperature thermal energy storage system. Energy conversion and management, 165, 477-487.

[16] Liang, Y., Chen, J., Luo, X., Chen, J., Yang, Z., & Chen, Y. (2020). Simultaneous optimization of combined supercritical CO2 Brayton cycle and organic Rankine cycle integrated with concentrated solar power system. Journal of Cleaner Production, 266, 121927.

[17] Sachdeva, J., & Singh, O. (2019). Thermodynamic analysis of solar powered triple combined Brayton, Rankine and organic Rankine cycle for carbon free power. Renewable Energy, 139, 765-780.

[18] Sadeghi, S., Ghandehariun, S., & Rezaie, B. (2021). Energy and exergy analyses of a solar-based multi-generation energy plant integrated with heat recovery and thermal energy storage systems. Applied Thermal Engineering, 188, 116629.

[19] Keshavarzzadeh, A. H., Ahmadi, P., & Rosen, M. A. (2020). Technoeconomic and environmental optimization of a solar tower integrated energy system for freshwater production. Journal of Cleaner Production, 270, 121760.

[20] Khatoon, S., & Kim, M. H. (2020). Performance analysis of carbon dioxide based combined power cycle for concentrating solar power. Energy Conversion and Management, 205, 112416.

[21] Yang, J., Yang, Z., & Duan, Y. (2020). Off-design performance of a supercritical CO2 Brayton cycle integrated with a solar power tower system. Energy, 201, 117676.

[22] Mohammadi, K., McGowan, J. G., & Saghafifar, M. (2019). Thermoeconomic analysis of multi-stage recuperative Brayton power cycles: Part I-hybridization with a solar power tower system. Energy Conversion and Management, 185, 898-919.

[23] Chitsaz, A., Haghghi, M. A., & Hosseinpour, J. (2019). Thermodynamic and exergoeconomic analyses of a proton exchange membrane fuel cell (PEMFC) system and the feasibility evaluation of integrating with a proton exchange membrane electrolyzer (PEME). Energy Conversion and Management, 186, 487-499.

[24] Haghghi, M. A., Holagh, S. G., Chitsaz, A., & Parham, K. (2019). Thermodynamic assessment of a novel multi-generation solid oxide fuel cell-based system for production of electrical power, cooling, fresh water, and hydrogen. Energy Conversion and Management, 197, 111895.

[25] Cao, Y., Dhahad, H. A., Sun, Y. L., Haghghi, M. A., Delpisheh, M., Athari, H., & Farouk, N. (2021). The role of input gas species to the cathode in the oxygen-ion conducting and proton conducting solid oxide fuel cells and their applications: Comparative 4E analysis. International Journal of Hydrogen Energy, 46(37), 19569-19589.

[26] Wang, L., Chen, M., Küngas, R., Lin, T. E., Diethelm, S., & Maréchal, F. (2019). Power-to-fuels via solid-oxide electrolyzer: Operating window and techno-economics. Renewable and Sustainable Energy Reviews, 110, 174-187.

[27] Iora, P., & Chiesa, P. (2009). High efficiency process for the production of pure oxygen based on solid oxide fuel cell–solid oxide electrolyzer technology. Journal of Power Sources, 190(2), 408-416.

[28] Delpisheh, M., Haghghi, M. A., Mehrpooya, M., Chitsaz, A., & Athari, H. (2021). Design and financial parametric assessment and optimization of a novel solar-driven freshwater and hydrogen cogeneration system with thermal energy storage. Sustainable Energy Technologies and Assessments, 45, 101096.

[29] Virkar, A. V. (2010). Mechanism of oxygen electrode delamination in solid oxide electrolyzer cells. International Journal of Hydrogen Energy, 35(18), 9527-9543.

[30] Holagh, S. G., Haghghi, M. A., & Chitsaz, A. (2022). Which methane-fueled fuel cell is of superior performance in CCHP applications; solid oxide or molten carbonate?. Fuel, 312, 122936.

[31] Stempien, J. P., Sun, Q., & Chan, S. H. (2013). Solid Oxide Electrolyzer Cell Modeling: A Review. Journal of Power Technologies, 93(4).

[32] Mohammadi, A., & Mehrpooya, M. (2018). Techno-economic analysis of hydrogen production by solid oxide electrolyzer coupled with dish collector. Energy Conversion and Management, 173, 167-178.

[33] Wang, F., Wang, L., Ou, Y., Lei, X., Yuan, J., Liu, X., & Zhu, Y. (2021). Thermodynamic analysis of solid oxide electrolyzer integration with engine waste heat recovery for hydrogen production. Case Studies in Thermal Engineering, 27, 101240.

[34] Hjeij, D., Biçer, Y., & Koç, M. (2022). Thermodynamic analysis of a multigeneration system using solid oxide cells for renewable power-to-X conversion. International Journal of Hydrogen Energy.

[35] Xu, Y. P., Lin, Z. H., Ma, T. X., She, C., Xing, S. M., Qi, L. Y., ... & Pan, J. (2022). Optimization of a biomass-driven Rankine cycle integrated with multi-effect desalination, and solid oxide electrolyzer for power, hydrogen, and freshwater production. Desalination, 525, 115486.

[36] Alirahmi, S. M., Assareh, E., Pourghassab, N. N., Delpisheh, M., Barelli, L., & Baldinelli, A. (2022). Green hydrogen & electricity production via geothermal-driven multi-generation system: Thermodynamic modeling and optimization. Fuel, 308, 122049.

[37] Xu, C., Wang, Z., Li, X., & Sun, F. (2011). Energy and exergy analysis of solar power tower plants. Applied Thermal Engineering, 31(17-18), 3904-3913.

[38] Linares, J. I., Montes, M. J., Cantizano, A., & Sánchez, C. (2020). A novel supercritical CO2 recompression Brayton power cycle for power tower concentrating solar plants. Applied Energy, 263, 114644.

[39] AlZahrani, A. A., & Dincer, I. (2016). Design and analysis of a solar tower based integrated system using high temperature electrolyzer for hydrogen production. international journal of hydrogen energy, 41(19), 8042-8056.

[40] Cao, Y., Dhahad, H. A., Togun, H., Haghghi, M. A., Anqi, A. E., Farouk, N., & Rosen, M. A. (2021). Seasonal design and multi-objective optimization of a novel biogas-fueled cogeneration application. International Journal of Hydrogen Energy, 46(42), 21822-21843.

[41] Cao, Y., Haghghi, M. A., Shamsaiee, M., Athari, H., Ghaemi, M., & Rosen, M. A. (2020). Evaluation and optimization of a novel geothermal-driven hydrogen production system using an electrolyser fed by a two-stage organic Rankine cycle with different working fluids. Journal of Energy Storage, 32, 101766.

[42] Haghghi, M. A., Mohammadi, Z., Pesteei, S. M., Chitsaz, A., & Parham, K. (2020). Exergoeconomic evaluation of a system driven by parabolic trough solar collectors for combined cooling, heating, and power generation; a case study. Energy, 192, 116594.

[43] Habibollahzade, A., Gholamian, E., Houshfar, E., & Behzadi, A. (2018). Multi-objective optimization of biomass-based solid oxide fuel cell integrated with Stirling engine and electrolyzer. Energy conversion and management, 171, 1116-1133.

[44] Delpisheh, M., Haghghi, M. A., Athari, H., & Mehrpooya, M. (2021). Desalinated water and hydrogen generation from seawater via a desalination unit and a low temperature electrolysis using a novel solar-based setup. international journal of hydrogen energy, 46(10), 7211-7229.

[45] Athari, H., Kiasatmanesh, F., Haghghi, M. A., Teymourzadeh, F., Yagoublou, H., & Delpisheh, M. (2022). Investigation of an auxiliary option to meet local energy demand via an innovative small-scale geothermal-driven system; a seasonal analysis. Journal of Building Engineering, 50, 103902.

[46] Moran, M. J., Shapiro, H. N., Boettner, D. D., & Bailey, M. B. (2010). Fundamentals of engineering thermodynamics. John Wiley & Sons.

[47] Bejan, A., Tsatsaronis, G., & Moran, M. J. (1995). Thermal design and optimization. John Wiley & Sons.